


Topology Optimization with Explicit Components Considering Stress Constraints

Yubao Ma ^{1,2} , Zhiguo Li ^{1,*}, Yuxuan Wei ^{1,2} and Kai Yang ^{1,2}¹ Xi'an Institute of Optics and Precision Mechanics of CAS, Xi'an 710119, China;

mayubao22@mailsucas.ac.cn (Y.M.); weiyuxuan@opt.ac.cn (Y.W.); yangkai2022@opt.ac.cn (K.Y.)

² School of Optoelectronics, University of Chinese Academy of Sciences, Beijing 100049, China

* Correspondence: lzg@opt.ac.cn

Abstract: Topology optimization focuses on the conceptual design of structures, characterized by a large optimization space and a significant impact on structural performance, and has been widely applied in industrial fields such as aviation and aerospace. However, most topology optimization methods prioritize structural stiffness and often overlook stress levels, which are critical factors in engineering design. In recent years, explicit topology optimization methods have been extensively developed due to their ability to produce clear boundaries and their compatibility with CAD/CAE systems. Nevertheless, research on incorporating stress constraints within the explicit topology optimization framework remains scarce. This paper is dedicated to investigating stress constraints within the explicit topology optimization framework. Due to the clear boundaries and absence of intermediate density elements in the explicit topology optimization framework, this approach avoids the challenge of stress calculation for intermediate density elements encountered in the traditional density method. This provides a natural advantage in solving topology optimization problems considering stress constraints, resulting in more accurate stress calculations. Compared with existing approaches, this paper proposes a novel component topology description function that enhances the deformability of components, improving the representation of geometric boundaries. The lower-bound Kreisselmeier–Steinhauser aggregation function is employed to manage the stress constraint, reducing the solution scale and computational burden. The effectiveness of the proposed method is demonstrated through two classic examples of topology optimization.



Citation: Ma, Y.; Li, Z.; Wei, Y.; Yang, K. Topology Optimization with Explicit Components Considering Stress Constraints. *Appl. Sci.* **2024**, *14*, 7171. <https://doi.org/10.3390/app14167171>

Academic Editor: Giangiacomo Minak

Received: 18 July 2024

Revised: 13 August 2024

Accepted: 13 August 2024

Published: 15 August 2024



Copyright: © 2024 by the authors. Licensee MDPI, Basel, Switzerland. This article is an open access article distributed under the terms and conditions of the Creative Commons Attribution (CC BY) license (<https://creativecommons.org/licenses/by/4.0/>).

Keywords: topology optimization; stress concentration; explicit components; stress aggregation function; method of moving asymptotes

1. Introduction

Since Bendsoe and Kikuchi proposed the topology optimization method based on homogenization theory [1] in 1988, the theoretical framework of continuum topology optimization has garnered significant attention from scholars. A series of effective topology optimization methods have subsequently emerged. Topology optimization has gradually become one of the most challenging subjects in structural mechanics.

Currently, topology optimization is primarily categorized into two main approaches. The first approach is based on material distribution, known as implicit topology optimization methods, and includes the solid isotropic material with penalization (SIMP) method [2] and the evolutionary structural optimization (ESO) method [3]. These methods utilize finite elements as independent design variables, which often result in the emergence of gray elements and jagged boundary issues, as illustrated in Figure 1a. Additionally, because the geometric description differs significantly from that of CAD modeling systems, the optimization results usually necessitate complex model reconstruction. The second approach is based on boundary descriptions and includes the level-set method (LSM) [4] and the moving morphable components (MMC)/voids (MMV) method [5,6]. These methods

directly capture structural boundary characteristics, thereby facilitating the acquisition of topological structures with smooth, well-defined boundaries, as depicted in Figure 1b.

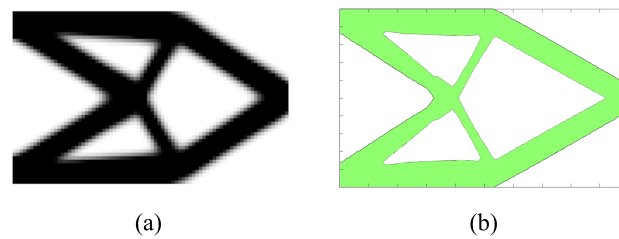


Figure 1. Comparison of two types of topology optimization methods applied to the short beam example. (a) Optimization results obtained using the implicit topology optimization method. (b) Optimization results obtained using the explicit topology optimization method.

However, although the level-set method is based on boundary descriptions, it utilizes a node-based implicit level-set function to describe the geometry, which significantly differs from the explicit geometric representation used in CAD modeling systems. Therefore, it is also considered an implicit topology optimization method. In 2014, Professor Xu Guo's team introduced the moving morphable components method, which employs a set of deformable components as building blocks for topology optimization. By optimizing the shape, orientation, and layout of these components, the optimal structural topology is identified. Since it utilizes the same explicit geometric representation as CAD modeling systems, the boundaries are explicitly extractable, and the optimization results can be directly integrated with CAD systems, pioneering the explicit topology optimization method. For further details on the development status of the MMC method, the authors recommend reading the review article in [7]. In recent years, many scholars have integrated implicit and explicit topology optimization methods to leverage the strengths of both, proposing a SIMP-MMC hybrid algorithm [8,9], as illustrated in Figure 2.

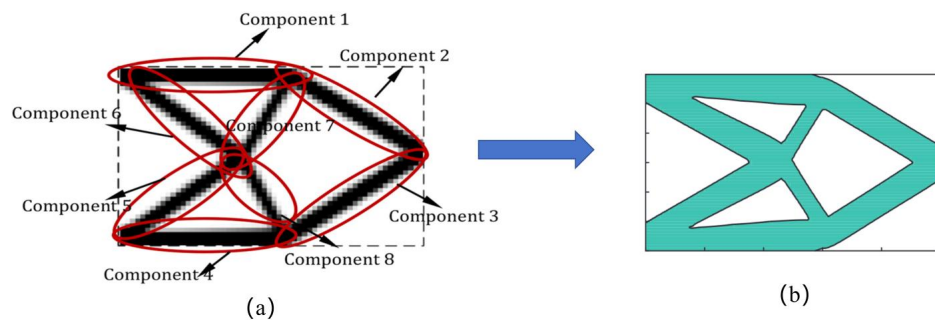


Figure 2. Schematic diagram illustrating the SIMP-MMC hybrid algorithm. (a) The initial force path, derived from the SIMP method, is extracted and mapped onto the component layout. (b) The final optimized result obtained using the MMC method [8].

By first utilizing the fast search capability of the SIMP method, the primary force transfer path of the structure can be identified after a few initial iterative steps. Subsequently, a contour extraction algorithm is employed to map the SIMP optimization results to the initial layout of the MMC components, thus addressing the issue of initial layout dependency in the MMC method and enhancing its solution speed and convergence stability.

However, incorporating stress constraints has consistently been a challenging issue in the field of topology optimization. Introducing stress constraints into the optimization model can lead to several significant challenges. Firstly, there is the phenomenon of stress singularities, which has been observed for many years in truss topology optimization designs involving stress constraints. Cheng and Jiang explained this phenomenon as due to the discontinuous nature of stress constraints, where optimization algorithms cannot completely eliminate some low-density areas, thus failing to achieve a genuinely optimal

topology [10]. Several effective methods have been proposed to address this issue, including ϵ -relaxation [11] and the smooth envelope function (SEF) [12]. Secondly, the local nature of stress constraints poses a considerable computational burden. The typical practice is to use aggregation functions to consolidate local stress constraints into a global constraint, significantly reducing the number of constraints. The constraint functions commonly applied in the literature include the Kreisselmeier–Steinhauser (KS) function [13] and the P-norm [14]. Additionally, the optimization method based on the SIMP model faces the challenge of defining stress constraints for intermediate-density elements. While stress constraints can be clearly defined for elements with relative densities of 0 or 1, defining stress constraints for intermediate-density material elements remains a topic of discussion. Most studies address this by establishing a stress interpolation function, characterizing it as the relationship between element stress and design variables. However, the form of the stress interpolation function directly affects the effectiveness of stress constraints, and applying such functions may make the optimized design more sensitive to initial designs and parameter selection, potentially increasing the uncertainty of optimization results.

To address these issues, researchers have extensively studied the L-shaped beam as a classic test case, as illustrated in Figure 3.

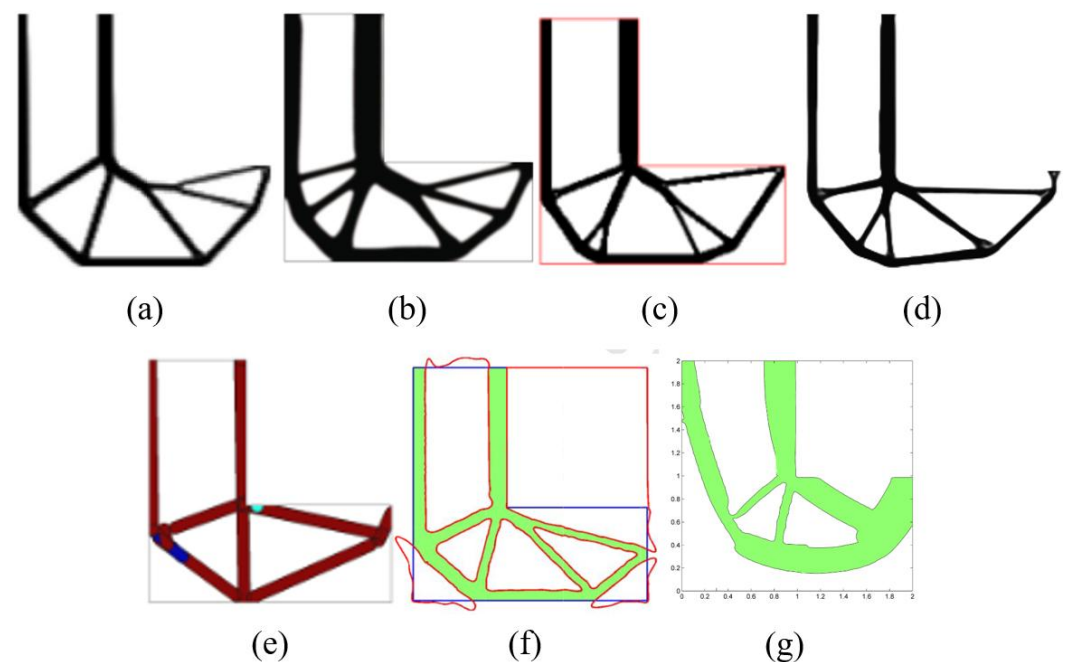


Figure 3. The designs of the L-shape beam in recent research. (a) Optimized result obtained by Dixiong Yang et al. using the implicit topology optimization method in 2018 [15]. (b) Optimized result obtained by Senhora et al. using the implicit topology optimization method in 2020 [16]. (c) Optimized result obtained by Xiaoya Zhai et al. using the implicit topology optimization method in 2021 [17]. (d) Optimized result obtained by Gustavo Assis da Silva et al. using the implicit topology optimization method in 2021 [18]. (e) Optimized result obtained by Shanglong Zhang et al. using the explicit topology optimization method in 2017 [19]. (f) Optimized result obtained by Weisheng Zhang et al. using the explicit topology optimization method in 2018 [20]. (g) Optimized result obtained by Pooya Rostami et al. using the explicit topology optimization method in 2021 [21].

Dixiong Yang et al. proposed a stress correction scheme based on the Stability Transformation Method (STM) and indicated that the KS stress function based on the STM exhibits a faster convergence rate in topology design [15], as demonstrated in Design A in the figure above. Senhora et al. introduced a method to effectively address stress constraint issues with a large number of constraints by modifying the penalty term and the objective function term of the augmented Lagrangian function [16], as shown in Design B. In Design C, Xiaoya

Zhai and colleagues adopted a similar concept and proposed an auxiliary stress variable linked to actual variables through equality constraints. The augmented Lagrangian format was utilized, combining the equality constraints into the objective function as linear and quadratic terms. The auxiliary stress variable and the density variable are treated as two sets of optimization variables, referred to as design and stress-alternating optimization [17]. Gustavo Assis da Silva et al. compared local and global stress constraint strategies in topology optimization. The global stress strategy is based on the P-mean aggregation function, and extensive parameter studies were conducted for L-shaped design problems [18], with one of the results shown in Design D.

Unlike the more mature developments in implicit topology optimization methods, explicit topology optimization methods considering stress constraints are still in their initial stages. Explicit topology optimization methods, characterized by geometric parametrization, allow for the explicit realization of structural boundaries with clear borders. This means that the problem of calculating stress in intermediate-density elements is avoided, offering significant potential to improve the accuracy of boundary stress calculations and reduce computational complexity. Shanglong Zhang et al. were the first to include stress constraints in structural topology optimization involving discrete geometric parts. By projecting the explicit and analytical geometric description of components onto a continuously varying density field, they inherited the convenience and advantages of density-based topology optimization [19], as shown in Design E. Weisheng Zhang et al. proposed a solution to the stress constraint problem based on the moving morphable voids method (MMV), achieving an optimized design with clear and explicitly parameterized boundaries using a limited number of finite-element analysis degrees of freedom and optimization variables [20], as seen in Design F. Design G was obtained by Pooya Rostami et al. They proposed a new component topology description function based on polar coordinates under the framework of the moving morphable components (MMC) method, which has a strong curve expression ability. Global and local volume constraints are introduced in the explicit topology optimization framework, which holds significant engineering relevance [21].

The primary focus of this paper is on addressing stress constraint issues using explicit topology optimization methods. Within the framework of the moving morphable components (MMC) method, a topology description function with robust deformation capability was developed, and the lower-bound Kreisselmeier–Steinhauser function was utilized to aggregate stress constraints. Compared to existing methods for topology optimization considering stress constraints, this paper avoids the issue of intermediate-density elements through the use of an explicit topology optimization method, resulting in more accurate stress calculations. Additionally, a new component topology description function with enhanced deformation capability is introduced to improve geometric representation. Furthermore, the ends of the components are curved to prevent issues such as sharp connections at straight ends, which can lead to stress concentration. The proposed method was proven effective in classical L-shaped and T-shaped beam case studies.

The structure of the remainder of the paper is as follows. Section 2 elaborates on the basic concept of the MMC method and the proposed topology description function. The formulation of the topology optimization problem and the aggregation treatment of stress constraints are presented in Section 3. Sensitivity analysis is conducted in Section 4. Representative examples are provided in Section 5, demonstrating the effectiveness of the method. Finally, a summary is provided in Section 6.

2. MMC Topology Optimization Framework and Geometrical Description

2.1. MMC Topology Optimization Method

The MMC method is a novel topology optimization framework proposed by Professor Guo Xu in 2014. The basic idea of this topology optimization method is illustrated in Figure 4. This method uses components described by explicit geometric information as structural primitives. By updating the design variables that control the movement and deformation of the components, the component layout is gradually optimized to achieve

the optimal structural configuration. Due to the parametric description of structural components used in the MMC method, the structural boundaries are clear and explicitly extractable, facilitating easy integration of the optimization results with CAD/CAE systems. Additionally, the design variables are a set of parameters that control the movement and deformation of the components, independent of the finite-element mesh. Compared with the SIMP method, the number of design variables is greatly reduced, improving solution efficiency.

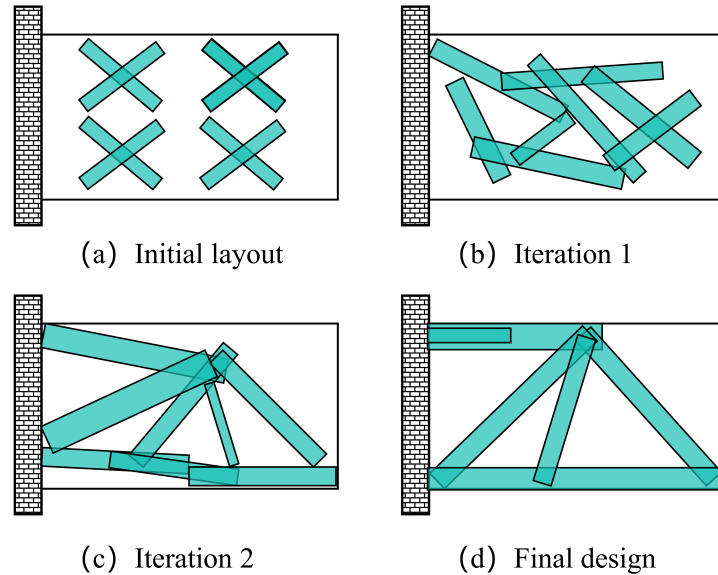


Figure 4. Schematic diagram of topology optimization of the short beam example based on the MMC method. (a) Initial layout of the components. (b) Movement and deformation of the components during the early stages of the optimization process. (c) Movement and deformation of the components during the later stages of the optimization process. (d) Optimized layout of the components.

Unlike the SIMP method, which describes material distribution through changes in element density, the MMC method describes material distribution through the topology description function (TDF) of the component.

$$\begin{cases} \Phi(x) > 0, & \text{if } x \in \Omega^s, \\ \Phi(x) = 0, & \text{if } x \in \partial\Omega^s, \\ \Phi(x) < 0, & \text{if } x \in D \setminus \Omega^s. \end{cases} \quad (1)$$

In Equation (1), x is a point in the design domain D , and Ω^s is the area occupied by the solid material component. There are n components in the design domain, and the global topology description function can be defined as $\Phi(x) = \max(\phi_1(x), \dots, \phi_i(x), \dots, \phi_n(x))$, $i = 1, \dots, n$, representing the component number. The topology description function of the i -th component is expressed as follows:

$$\begin{cases} \phi_i(x) > 0, & \text{if } x \in \Omega_i, \\ \phi_i(x) = 0, & \text{if } x \in \partial\Omega_i, \\ \phi_i(x) < 0, & \text{if } x \in D \setminus \Omega_i. \end{cases} \quad (2)$$

In Equation (2), Ω_i is the area occupied by the i -th component. Since the pioneering work of Professor Guo Xu in 2014, many scholars have proposed various component topology description functions [22–26]. These functions have the ability to deform in different directions and dimensions, enhancing the expression of geometric boundaries and enabling the algorithm to search for the optimal structure more freely.

However, if the end of the component is a straight line, it will lead to some inevitable problems. As shown in Figure 5, in the intersection area of the components, the boundary can become difficult to express. Additionally, the internal angle where the components connect should ideally be a smooth curve to reduce stress concentration, but this is difficult to achieve with components that have a straight end.

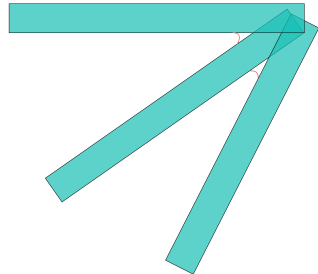


Figure 5. Schematic diagram of component connection at the end of a straight line.

2.2. A New Topology Description Function

To address the above-mentioned problems, this paper proposes a new component topology description function. Compared with those proposed by Guo and Zhang [27], the straight line at the end of the component in this function can be bent and deformed, greatly enhancing the component’s deformation ability. The mathematical model of this component topology description function can be expressed as follows:

$$\phi_i(x, y) = \left(\frac{x'}{g(y')} \right)^m + \left(\frac{y'}{f(x')} \right)^m - 1, \tag{3}$$

$$\begin{Bmatrix} x \\ y \end{Bmatrix} = \begin{bmatrix} \cos\theta_i & \sin\theta_i \\ -\sin\theta_i & \cos\theta_i \end{bmatrix} \begin{Bmatrix} x - x_{0i} \\ y - y_{0i} \end{Bmatrix}, \tag{4}$$

In Equation (3), $\phi_i(x, y)$ represents a superellipse level-set function, where m is a parameter controlling the shape of the superellipse. By adjusting the value of m , various shapes, ranging from a circle to a rectangle, can be generated and described. As m approaches infinity, the superellipse approximates a rectangle [28]. Building upon the research of various pioneers [5,27,29], we select $m = 6$ in this paper. Equation (4) is used for coordinate transformation to convert the global coordinate to the local coordinate of the component. (x_{0i}, y_{0i}) is the central coordinate of the i -th component, and θ_i is the inclination angle of the i -th component. The shape of the component is jointly controlled by $f(x')$ and $g(y')$, as shown in Equations (5) and (6).

$$f(x') = \frac{t_{i1} + t_{i2} - 2t_{i3}}{2l_{i1}^2}x'^2 + \frac{t_{i2} - t_{i1}}{2l_{i1}}x' + t_{i3}, \tag{5}$$

$$g(y') = \begin{cases} \sqrt{r_i^2 - (y' - y_{0i}^r)^2} + x_{0i}^r, & \text{if } l_{i1} < l_{i2}, \\ l_{i1}, & \text{if } l_{i1} = l_{i2}, \\ -\sqrt{r_i^2 - (y' - y_{0i}^r)^2} + x_{0i}^r, & \text{if } l_{i1} > l_{i2}. \end{cases} \tag{6}$$

In Equation (5), t_{i1}, t_{i2} , and t_{i3} are half of the thicknesses at three positions of the component, l_{i1} is half of the length on the central axis of the component, and l_{i2} is half of the length on both sides of the component, as shown in Figure 6. Here, we assume that the lengths on both sides of the component are equal. (x_{0i}^r, y_{0i}^r) and r_i are the central coordinates and radius of the arc at the end of the i -th component, respectively. They can be calculated as follows:

$$\begin{cases} x_{0i}^r = \frac{l_{i1}^2}{2(l_{i2}-l_{i1})}, & r_i^2 = (x_{0i}^r + l_{i2})^2 + (y_{0i}^r + t_{i1})^2. \\ y_{0i}^r = \frac{l_{i2}^2 + t_{i1}^2}{2}, \end{cases} \quad (7)$$

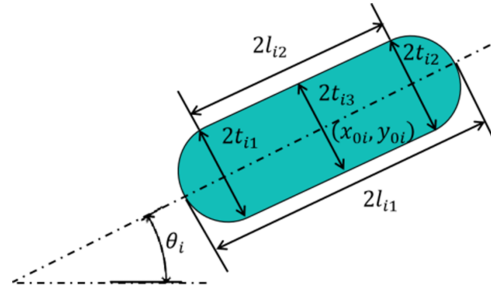


Figure 6. Parametric description of the variability of the shape of the components.

In this way, each component has eight variables $(x_0, y_0, l_1, l_2, t_1, t_2, t_3, \theta)$, and by optimizing the values of these variables, the movement and deformation of the component can be controlled. As shown in Figure 7, different variable values result in various component shapes (the variables $[l_1, l_2, t_1, t_2, t_3]$ controlling the length and thickness of the component take values of (a) $[0.09, 0.05, 0.07, 0.11, 0.09]$, (b) $[0.09, 0.05, 0.09, 0.09, 0.11]$, (c) $[0.09, 0.05, 0.11, 0.07, 0.09]$, (d) $[0.05, 0.09, 0.09, 0.09, 0.05]$, and (e) $[0.09, 0.09, 0.09, 0.09, 0.09]$). It can be observed that this TDF effectively enhances the deformation ability of the component.

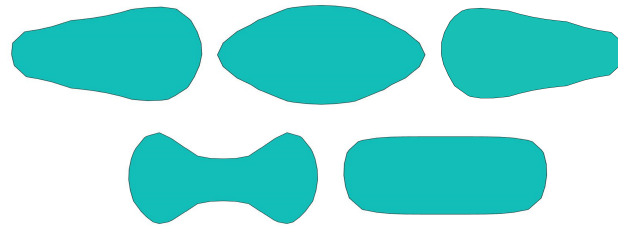


Figure 7. Component deformation diagrams with different parameters.

3. Problem Formulation

3.1. Problem Statement and Mathematical Formulation

The compliance minimization problem with global stress constraints and global volume constraints can be expressed as shown in Equation (8).

$$\begin{cases} \text{Find } \mathbf{D}_g = ((\mathbf{D}_1)^T, (\mathbf{D}_2)^T, \dots, (\mathbf{D}_n)^T)^T, \\ \min : C = \int_D H(\Phi(\mathbf{x}, \mathbf{D}_g)) f^j \cdot \mathbf{u} dV + \int_{\Gamma_t} \mathbf{t} \cdot \mathbf{u} dS, \\ \text{s.t.} \\ \sum_{j=1}^n \int_D H(\Phi(\mathbf{x}, \mathbf{D}_g)) \tilde{\mathbf{E}} : \boldsymbol{\varepsilon}(\mathbf{u}) : \boldsymbol{\varepsilon}(\mathbf{v}) dV \\ \quad = \int_D H(\Phi(\mathbf{x}, \mathbf{D}_g)) \mathbf{f} \cdot \mathbf{v} dV + \int_{\Gamma_t} (\Phi(\mathbf{x}, \mathbf{D}_g)) \mathbf{t} \cdot \mathbf{v} dS, \forall \mathbf{v} \in u_{ad}, \\ \int_D H(\Phi(\mathbf{x}; \mathbf{D}_g)) dV \leq \bar{V}, \\ g(\mathbf{u}, \mathbf{D}_g) \leq 0, \\ D \subset u_D, \mathbf{u} = \bar{\mathbf{u}}, \text{ on } \Gamma_u \end{cases} \quad (8)$$

In the above equation, \mathbf{D}_g is the vector of the global design variables for all components (n components) in the design domain. f^j and \mathbf{t} are the volume force and surface traction, respectively, and \mathbf{u} and \mathbf{v} are the displacement fields. $\bar{\mathbf{u}}$ is the prescribed displacement on the Dirichlet boundary Γ_u . The Neumann boundary condition is represented as Γ_t . $\boldsymbol{\varepsilon}$ represents the second-order linear strain tensor. In this formula, $\tilde{\mathbf{E}} = E/(1 + \nu)[\mathbf{I} + \nu/(1 - 2\nu)\boldsymbol{\delta} \otimes \boldsymbol{\delta}]$, where E is the Young's modulus, ν is the Poisson's ratio, and \mathbf{I} and $\boldsymbol{\delta}$ represent the

fourth-order and second-order unit tensors of the identity, respectively. Φ is the topology description function of all components mentioned in Section 2, \bar{V} is the prescribed global volume constraint, and $g(\mathbf{u}, \mathbf{D}_g)$ is the prescribed global stress constraint, which is discussed in detail in the subsequent sections. The Heaviside function used in Equation (8) is defined as follows:

$$H(\phi) = \begin{cases} 1 & \phi > \lambda \\ \frac{3(1-\xi)}{4} \left(\frac{\phi}{\lambda} - \frac{\phi^3}{3\lambda^3} \right) + \frac{1+\xi}{2} & -\lambda \leq \phi \leq \lambda \\ \xi & \text{else} \end{cases} \quad (9)$$

In Equation (9), λ and ξ are parameters that control regularization and singularity, respectively. The finite-element analysis unit in this paper adopts the widely used four-node rectangular element and uses the ersatz material model [30] to obtain the Young’s modulus of the element by interpolating the TDF values at the four nodes of the element as follows:

$$E^e = \frac{E \left(\sum_{i=1}^4 (H(\phi_i^e))^q \right)}{4}, \quad (10)$$

Equation (10) establishes the relationship between the geometric model and the finite-element model, where E^e is the Young’s modulus of the element e . E is the Young’s modulus of the solid material. $\phi_i^e, i = 1, \dots, 4$, represents the values of the TDF at the four nodes of element e , and q is the penalty parameter, typically chosen as $q \geq 1$ [30]. In the present study, the value of q is set to 2 in accordance with established research precedents [24,25,31]. This treatment greatly enhances computational efficiency, thereby reducing computational costs.

3.2. Global Stress Control

In the studies of other pioneering researchers, most stress constraints are as follows:

$$g_j = \frac{|\sigma_j|}{\sigma_{lim}} - 1 \leq 0, \quad 1 \leq j \leq n_e \quad (11)$$

In Equation (11), σ_{lim} is the stress limit of the structure, and n_e is the number of solid elements. To address the difficulties caused by considering the stress constraint problem mentioned in Section 1, this paper uses the well-known lower-bound KS aggregation model. Alexander Verbart et al. proved that using the lower-bound KS function can be considered a special case of using the original upper-bound KS function to aggregate constraints combined with ε – relaxation, and thus, no additional relaxation techniques are required [32]. They pointed out that the value in the aggregation parameter $P \in [20, 40]$ can achieve the best results. The lower-bound KS function is expressed as follows:

$$\Psi_{KS}^L = \Psi_{KS}^U - \frac{1}{P} \ln(N) = \frac{1}{P} \ln \left(\frac{1}{N} \sum_{i=1}^N e^{P \bar{g}_i} \right). \quad (12)$$

In the above equation, P represents the aggregation parameter, and N denotes the number of elements. Utilizing Equation (12), we can reformulate the global stress constraint described in Equation (11) accordingly.

$$g_j = \frac{1}{P} \ln \left(\frac{1}{N} \sum_{i=1}^N e^{P \bar{g}_i} \right) \leq 0, \quad (13)$$

where

$$\bar{g}_i = H(\Phi(\mathbf{x}; \mathbf{D}_g)) \left(\frac{\sigma_{VM,i}}{\sigma_{lim}} - 1 \right) \quad (14)$$

In Equation (14), $\sigma_{VM,i}$ is the von Mises stress calculated at the center of the i -th element, which is defined as follows:

$$\sigma_{VM,i} = \left(\sigma_i^T V \sigma_i \right)^{1/2}, \tag{15}$$

where

$$V = \begin{pmatrix} 1 & -1/2 & 0 \\ -1/2 & 1 & 0 \\ 0 & 0 & 3 \end{pmatrix} \tag{16}$$

$$\sigma_i = C_0 B u_i \tag{17}$$

$\sigma_i = C_0$ is the stress–strain matrix related to Young’s modulus E and Poisson’s ratio, B is the strain-displacement matrix, and u_i is the displacement vector of the i -th element.

4. Sensitivity Analysis

In this paper, the method of moving asymptotes (MMA) is selected as the nonlinear optimization solver. Since the design variables in the components can be accurately described, the sensitivity values of the objective function and the volume constraint function are similar to those solved in the literature [5,27,29,33,34], and are not discussed in detail in this paper. The corresponding variable sensitivity value of $g(y')$ in the constructed TDF (taking $l_{i1} < l_{i2}$ as an example) can be expressed as follows:

$$\frac{\partial g(y')}{\partial x_0} = - \frac{\sin \theta_i (y' - y_{0i}^r)}{\sqrt{r_i^2 - (y' - y_{0i}^r)^2}} \tag{18}$$

$$\frac{\partial g(y')}{\partial y_0} = \frac{\cos \theta_i (y' - y_{0i}^r)}{\sqrt{r_i^2 - (y' - y_{0i}^r)^2}} \tag{19}$$

$$\frac{\partial g(y')}{\partial l_1} = \frac{l_{i1} l_{i2} (x_{0i}^r + l_{i2})}{(l_{i2} - l_{i1})^2 \sqrt{r_i^2 - (y' - y_{0i}^r)^2}} + \frac{l_{i1} l_{i2}}{(l_{i2} - l_{i1})^2} \tag{20}$$

$$\frac{\partial g(y')}{\partial l_2} = \frac{(x_{0i}^r + l_{i2}) \left(1 - \frac{l_{i1}^2}{2(l_{i2} - l_{i1})^2} \right) + l_{i2} (t_{i1} + y')}{\sqrt{r_i^2 - (y' - y_{0i}^r)^2}} - \frac{l_{i1}^2}{2(l_{i2} - l_{i1})^2} \tag{21}$$

$$\frac{\partial g(y')}{\partial t_1} = \frac{y_{0i}^r + t_{i1} (y' - y_{0i}^r + 1)}{\sqrt{r_i^2 - (y' - y_{0i}^r)^2}} \tag{22}$$

$$\frac{\partial g(y')}{\partial \theta} = \frac{(y' - y_{0i}^r) [\cos \theta_i (x - x_{0i}) + \sin \theta_i (y - y_{0i})]}{\sqrt{r_i^2 - (y' - y_{0i}^r)^2}} \tag{23}$$

The derivation process of the variable sensitivity value corresponding to the global stress constraint is as follows:

$$\frac{\partial \sigma_{VM}}{\partial \sigma} = \frac{1}{2} (\sigma^T V \sigma)^{-\frac{1}{2}} 2 \sigma^T V = \sigma_{VM}^{-1} \sigma^T V, \tag{24}$$

$$\frac{\partial \sigma_{VM}}{\partial d} = \frac{\partial \sigma_{VM}}{\partial \sigma} \frac{\partial \sigma}{\partial d} = \sigma_{VM}^{-1} \sigma^T V \frac{\partial \sigma}{\partial d} \tag{25}$$

$$\frac{\partial \sigma_{VM}}{\partial d} = \frac{1}{4} \sigma_{VM}^{-1} \sigma^T V E B L \sum_{e=1}^n \sum_{i=1}^4 H(\phi_i^e) \frac{\partial U}{\partial d}, \tag{26}$$

In Equation (26), L is the selection vector used to extract the corresponding displacement vector of the cell from the global displacement vector. The term $\frac{\partial U}{\partial d}$ can be derived from the balance equation $F = KU$ by taking a partial derivative with respect to d .

$$\frac{\partial U}{\partial d} = -K^{-1} \frac{\partial K}{\partial d} U, \tag{27}$$

$$K = \sum_{i=1}^{NE} K_e E_e = \sum_{i=1}^{NE} \sum_{j=1}^4 K_e \frac{E(H(\phi_j^e))^q}{4}, \tag{28}$$

In the above equation, the expression for the global stiffness matrix K is calculated. k_e represents the element stiffness matrix, and E_e denotes the Young’s modulus of the element, as determined in Equation (10). Substituting Equation (28) into Equation (27) yields the following result:

$$\frac{\partial U}{\partial d} = -\left(E \sum_{e=1}^{NE} \sum_{i=1}^4 k_e \frac{H(\phi_i^e)^q}{4}\right)^{-1} \left(E \sum_{e=1}^{NE} \sum_{i=1}^4 k_e q \frac{\partial H(\phi_i^e)}{\partial d} \frac{H(\phi_i^e)^{q-1}}{4}\right) U, \tag{29}$$

By substituting Equation (29) into Equation (26), we obtain

$$\frac{\partial \sigma_{VM,i}}{\partial d} = \frac{1}{4} \sigma_{VM,i}^{-1} \sigma_i^T \text{VEB}_i L_i \sum_{e=1}^{NE} \sum_{i=1}^4 H(\phi_i^e) \left[-\left(E \sum_{e=1}^{NE} \sum_{i=1}^4 k_e \frac{H(\phi_i^e)^q}{4}\right)^{-1} \left(E \sum_{e=1}^{NE} \sum_{i=1}^4 k_e q \frac{\partial H(\phi_i^e)}{\partial d} \frac{H(\phi_i^e)^{q-1}}{4}\right) U \right], \tag{30}$$

Upon deriving the above equation, the sensitivity of the global stress constraint function can be streamlined using the following adjoint equation:

$$K\lambda = \sigma_{VM,i}^{-1} \sigma_i^T \text{VEB}_i L_i \frac{\left(\sum_{e=1}^{NE} \sum_{i=1}^4 H(\phi_i^e(x))\right) \frac{\sigma_{VM}}{\sigma_{lim}} \exp\left(p\left(\sum_{e=1}^{NE} \sum_{i=1}^4 H(\phi_i^e(x))\right) \left(\frac{\sigma_{VM}}{\sigma_{lim}} - 1\right)\right)}{\sum_{i=1}^N \exp\left(p\left(\frac{\sigma_{VM}}{\sigma_{lim}} - 1\right)\right)}, \tag{31}$$

The sensitivity of the global stress constraint function can be expressed as follows:

$$\frac{\partial g}{\partial d} = \frac{\left(\frac{\sigma_{VM}}{\sigma_{lim}} - 1\right) \exp\left(p\left(\frac{\sigma_{VM}}{\sigma_{lim}} - 1\right) \sum_{e=1}^{NE} \sum_{i=1}^4 H(\phi_i^e(x))\right)}{\sum_{i=1}^N \exp\left(p\left(\frac{\sigma_{VM}}{\sigma_{lim}} - 1\right)\right)} + \frac{1}{4} \lambda \sum_{e=1}^{NE} \sum_{i=1}^4 H(\phi_i^e) \left[\left(E \sum_{e=1}^{NE} \sum_{i=1}^4 k_e q \frac{\partial H(\phi_i^e)}{\partial d} \frac{H(\phi_i^e)^{q-1}}{4}\right) U \right], \tag{32}$$

5. Numerical Solution Aspects

In this paper, two classical cases of L-shaped and T-shaped beams are used to test the effectiveness of the proposed method. In every instance, the material properties, load parameters, and geometric data are selected to be dimensionless, as the primary objective of this study is to evaluate the numerical performance of the proposed algorithm. The Young’s modulus E of the material is 1, and the Poisson’s ratio ν is 0.3. In the two cases, the aggregation parameter is set to $P = 20$. The calculation platform uses the MATLAB R2019a version, with an Intel i5 CPU and 16 GB of RAM (Intel, Santa Clara, CA, USA). The MMA optimizer code used was proposed by Svanberg [35], and its parameter settings are shown in the Table 1.

Table 1. MMA optimizer parameter settings.

epsimin	raa0	albafa	asyinit	asyincr	asydecr
10^{-10}	0.01	0.4	0.1	0.8	0.6

5.1. L-Shaped Beam

The design domain and boundary conditions of the L-shaped beam example are shown in Figure 8a. A fixed constraint is applied to the top of the beam, and a downward force $F = 1$ is applied to the center of the right side. Obviously, stress concentration will

occur in the right-angle area. The finite-element analysis uses a four-node rectangular bilinear element with an element size of 0.025 and a total of 4096 elements.

Components are essential as the fundamental building blocks of the MMC method. With a smaller number of components, the limited descriptive ability of the geometry may fail to identify effective force transfer paths, causing the optimization process to oscillate significantly and leading to non-convergence. Conversely, a higher number of components introduces a large number of design variables, resulting in excessive computational demand. Considering both convergence and computational efficiency, this paper adopts 16 components. The initial layout of the components is shown in Figure 8b, and the initial parameters of each component are set to $ini_val = [0.33 \ 0.20 \ 0.08 \ 0.08 \ 0.04]$. In addition, each component also includes three parameters representing the position and angle, for a total of 8 parameters. Thus, the solution dimension of the problem is 128 design variables. The value of the upper limit of the global volume constraint is set to $\bar{V} = 0.4$, and the upper limit value of the global stress constraint is set to $\delta_{lim} = 70$, which is the same as the setting in some other literature [15,36].

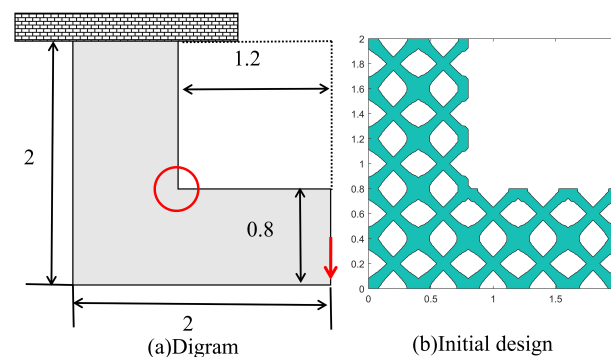


Figure 8. The design area and the initial layout of the components of the L-shaped beam.

Figure 9d shows the final result of the optimization. After approximately 70 iterations, it converges stably, satisfying the volume constraint and the global stress constraint, with the minimum compliance being 178.288. Benefiting from the advantage that the MMC method can be directly integrated into the CAD/CAE system, the geometric boundary information is transmitted to ABAQUS. Based on the method mentioned in ABAQUS [37], the obtained geometric boundary, the created finite-element mesh (a hybrid mesh dominated by quadrilaterals with an element size of 0.025, consisting of 1622 elements in Figure 9b and 1703 elements in Figure 9e), and the plotted von Mises stress distribution are shown in Figure 9. These results compare scenarios with and without considering the stress constraint.

From the analysis results in Figure 9, it is evident that after adding the global stress constraint, the angle at the corner of the L-shaped beam becomes larger, and the stress concentration at the corner is significantly improved. While maintaining structural stiffness (the structural compliance only increases by 7.23%, from 166.261 to 178.288), the local maximum stress value of the structure is significantly reduced (the maximum von Mises stress value is reduced by 49.47%, from 137.640 to 69.548). Additionally, the overall stress distribution of the structure is more uniform. The iterative convergence curves of the objective function and the constraint function are shown in Figure 10.

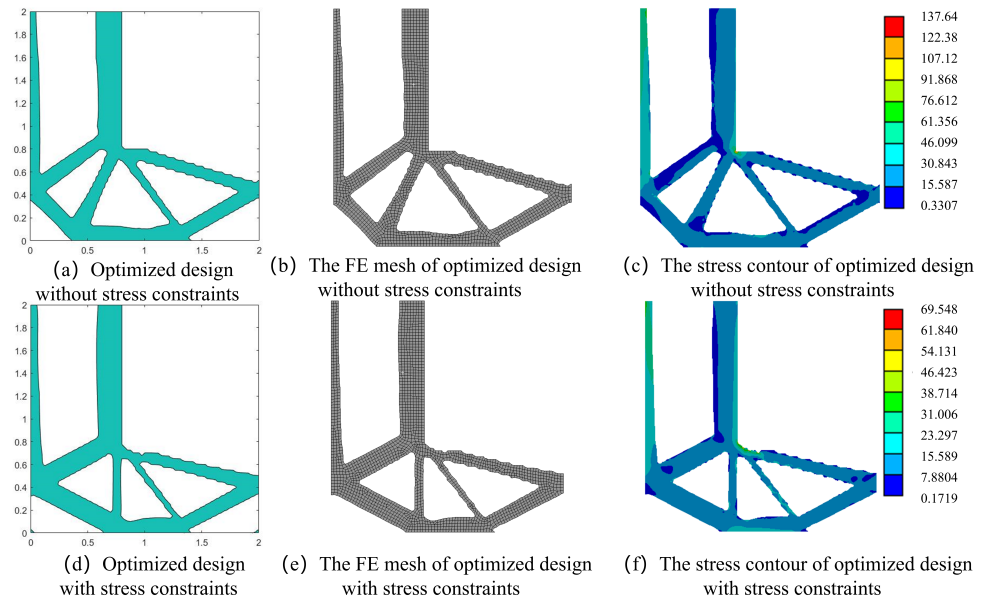


Figure 9. Comparison of the optimization results before and after adding stress constraints, including the finite-element mesh and stress distribution calculated from ABAQUS.

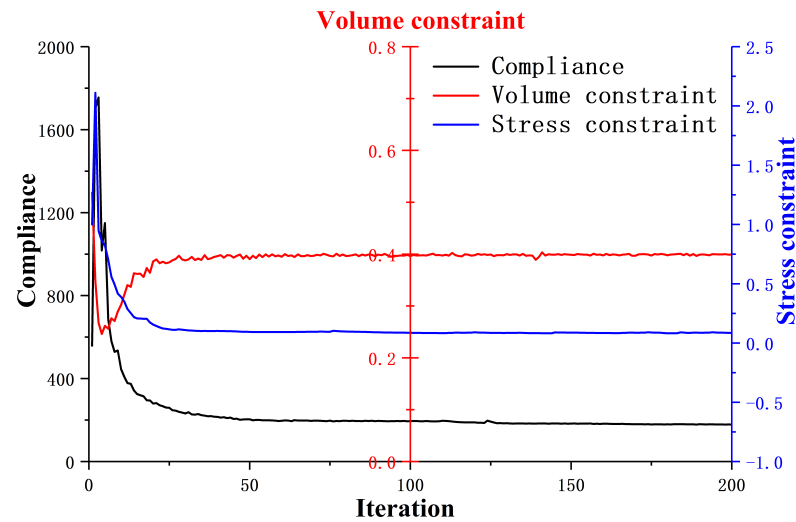


Figure 10. The iterative convergence curves of the objective function and the constraint function of the L-shaped beam.

The iterative curve shows that in the early stages of optimization, the components search for the optimal structural form with large-scale movement and deformation, causing significant oscillations in the objective function and the constraint function. However, the compliance of the structure exhibits an overall downward trend. As optimization progresses, the objective function and the constraint function gradually stabilize and converge. Some key iterative steps in the optimization process are shown in Figure 11.

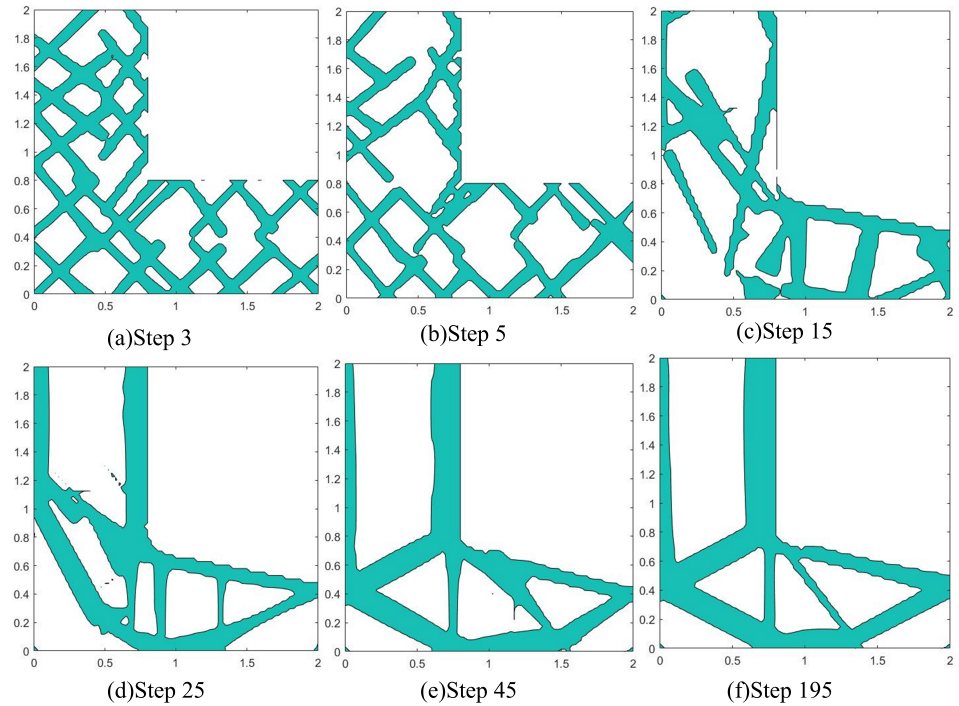


Figure 11. Some key iterative steps in the optimization process of the L-shaped beam

5.2. T-Shaped Beam

To further test the effectiveness of the algorithm, this paper selects a T-shaped beam with symmetrical load and boundary conditions as an example, as shown in Figure 12a. The upper end of the T-shaped beam is fixed, and a downward force $F = 1N$ is applied at the center of both ends of the beam. Similar to the L-shaped beam, stress concentration will occur at the two right-angle corners. Because the boundary conditions and loads of the beam are symmetrical, it can be predicted that the optimized structure will also exhibit symmetry, thereby further testing the feasibility and convergence of the algorithm. Similarly, the finite-element analysis uses a four-node rectangular bilinear element with an element size of 0.025, totaling 5632 elements.

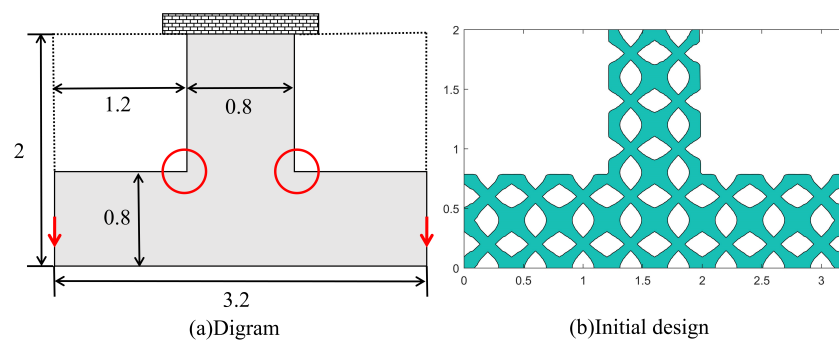


Figure 12. The design area and the initial layout of the components of the T-shaped beam.

Using the same initial values of the components as mentioned above ($ini_val = [0.33, 0.20, 0.08, 0.08, 0.04]$), a total of 22 components are used, and the initial layout of the components is shown in Figure 12b, with a total of 176 design variables. After approximately 100 iterations, it converges stably, and the final result of the optimization is shown in Figure 13d, with a minimum compliance of 164.125. Using the same treatment method as mentioned above (a hybrid mesh dominated by quadrilaterals with an element size of 0.025, consisting of 2187 elements in Figure 13b and 2246 elements in Figure 13e), the optimization result is compared with the result obtained without adding stress constraints.

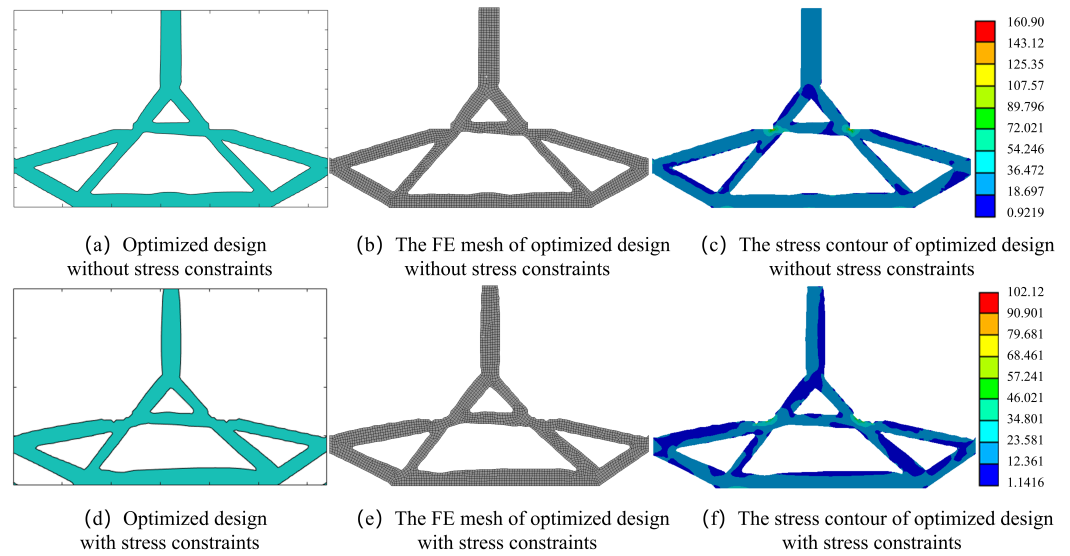


Figure 13. Comparison of the optimization results before and after adding stress constraints, including the finite-element mesh and stress distribution calculated from ABAQUS.

After adding the stress constraint, the angles at the right-angle corners on both sides of the T-shaped beam become gentler, and the stress concentration phenomenon is significantly improved. Additionally, the structure still maintains a high degree of symmetry. While maintaining the stiffness of the structure (the structural compliance only increases by 6.69%, from 164.125 to 175.108), the overall stress level is greatly reduced (the maximum von Mises stress is reduced by 57.56%, from 160.900 to 102.120). The iterative curves of the objective function and the constraint function for this case are shown in Figure 14.

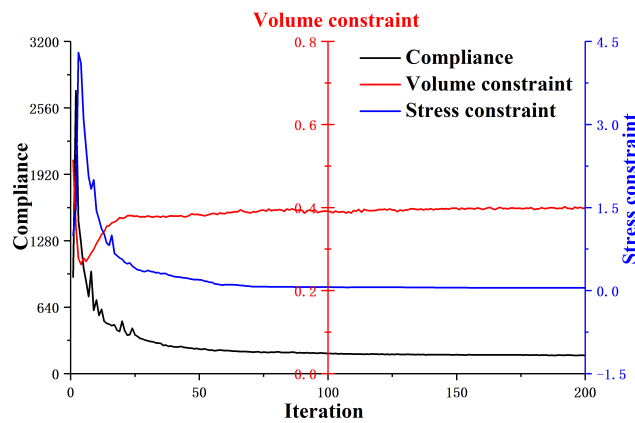


Figure 14. The iterative convergence curves of the objective function and the constraint function of the T-shaped beam.

As shown in Figure 14, after the initial stage of component movement and deformation, both the objective function and the constraint function accurately converge. Compared with the iterative process of the L-shaped beam, the T-shaped beam has more complex working conditions, resulting in a relatively slower speed of iterative convergence. Some key iterative steps in the optimization process are shown in Figure 15.

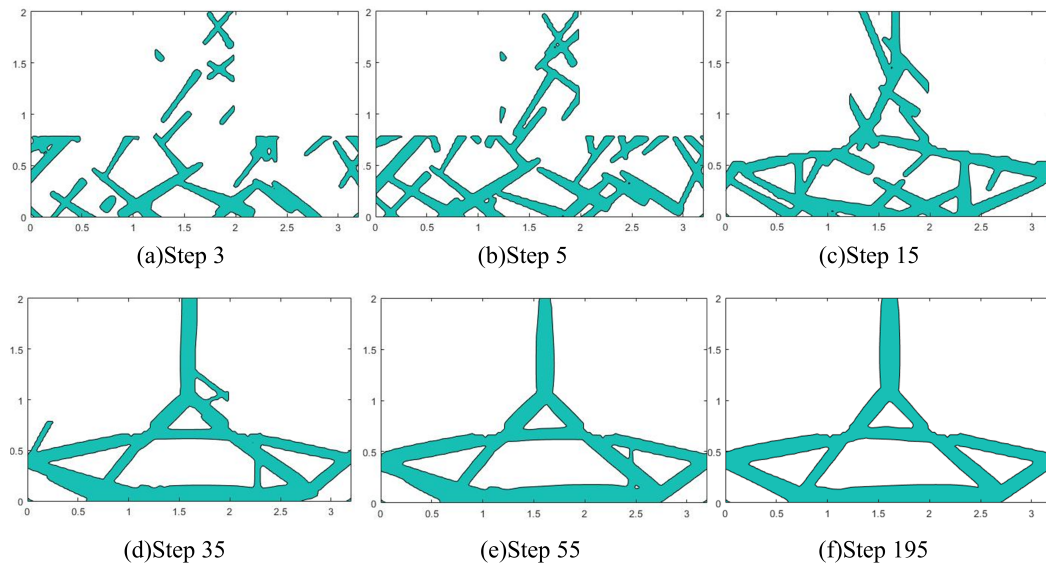


Figure 15. Some key iterative steps in the optimization process of the T-shaped beam.

6. Conclusions

This paper proposes a two-dimensional topology optimization scheme that considers global stress constraints within the framework of the MMC method. A novel topology description function for the component is proposed, enhancing its deformation ability. Compared to a component with a straight-line end, this function provides a better and more reasonable representation of the geometric boundary at the intersection of the components. The global stress constraint is managed using the lower-bound KS aggregation function, and the proposed method is validated through two classical numerical examples. In the two classical numerical examples, while maintaining structural stiffness, the increase in the compliance value does not exceed 8%, and the maximum von Mises stress is reduced by about 50%, successfully addressing the stress concentration issue. In addition, the overall stress distribution is more uniform. However, the authors observed some unsmooth, sawtooth-shaped boundary phenomena in the fillet expression, which may require introducing functions within the framework to smooth the boundary. As described in the literature [8], the minimum size of the structure is precisely controlled by setting the minimum spacing between the end features of the components to ensure their complete connection. Furthermore, the use of non-uniform rational B-spline (NURBS) curves or other advanced curve-fitting techniques to describe component boundaries, along with improvements to existing topology description functions to further enhance the geometrical descriptive capability of the components, should also be considered. Additionally, during the debugging process, the authors found that the MMC method is highly dependent on the initial values of the component variables, the initial layout, and certain parameters in the MMA algorithm. Some empirical changes may worsen the convergence of the algorithm. Combining parameter selection with existing intelligent algorithms, such as deep learning, might achieve better results. Similar ideas can be found in the literature [38]. The current research aims to preliminarily address stress constraints within the explicit topology optimization framework, demonstrating the substantial potential of explicit topology optimization methods in tackling stress-related challenges through two classical examples. Future research should focus on effectively mitigating stress concentration within the MMC framework to achieve smoother boundary representations and on developing a rational parameter selection mechanism to enhance optimization efficiency, both of which remain challenging and significant topics. From the perspective of the authors, addressing the challenges identified in existing studies by introducing advanced boundary description methods, optimization algorithms, and parameter-tuning techniques could be highly promising. Future research will further explore these aspects

to enhance practical applicability in engineering, thereby advancing the field of structural topology optimization.

Author Contributions: Conceptualization, Y.M.; methodology, Y.M.; software, Y.M.; validation, Y.W. and K.Y.; formal analysis, Z.L.; investigation, Y.M.; resources, Z.L.; data curation, Y.M. and K.Y.; writing—original draft preparation, Y.M.; writing—review and editing, Y.M. and K.Y.; visualization, Y.M.; supervision, Z.L. and Y.W.; project administration, Y.M. All authors have read and agreed to the published version of the manuscript.

Funding: This research received no external funding.

Institutional Review Board Statement: Not applicable.

Informed Consent Statement: Not applicable.

Data Availability Statement: The data that support the findings of this study are available from the authors upon reasonable request.

Conflicts of Interest: The authors declare no conflicts of interest.

Abbreviations

The following abbreviations are used in this manuscript:

SIMP	Solid isotropic material with penalization
LSM	Level-set method
ESO	Evolutionary structural optimization
MMC	Moving morphable components
MMA	Method of moving asymptotes
TDF	Topology description function

References

- Bendsøe, M.P.; Kikuchi, N. Generating optimal topologies in structural design using a homogenization method. *Comput. Methods Appl. Mech. Eng.* **1988**, *71*, 197–224. [[CrossRef](#)]
- Bendsøe, M.P.; Sigmund, O. Material interpolation schemes in topology optimization. *Arch. Appl. Mech.* **1999**, *69*, 635–654. [[CrossRef](#)]
- Querin, O.M.; Young, V.; Steven, G.; Xie, Y. Computational efficiency and validation of bi-directional evolutionary structural optimisation. *Comput. Methods Appl. Mech. Eng.* **2000**, *189*, 559–573. [[CrossRef](#)]
- Wang, M.Y.; Wang, X.; Guo, D. A level set method for structural topology optimization. *Comput. Methods Appl. Mech. Eng.* **2003**, *192*, 227–246. [[CrossRef](#)]
- Guo, X.; Zhang, W.; Zhong, W. Doing topology optimization explicitly and geometrically—A new moving morphable components based framework. *J. Appl. Mech.* **2014**, *81*, 081009. [[CrossRef](#)]
- Zhang, W.; Yang, W.; Zhou, J.; Li, D.; Guo, X. Structural topology optimization through explicit boundary evolution. *J. Appl. Mech.* **2017**, *84*, 011011. [[CrossRef](#)]
- Li, Z.; Xu, H.; Zhang, S. A Comprehensive Review of Explicit Topology Optimization Based on Moving Morphable Components (MMC) Method. *Arch. Comput. Methods Eng.* **2024**, *31*, 1–30. [[CrossRef](#)]
- Ruichao, L.; Shikai, J.; Ying, L.; Dengbao, X.; Yang, C. A Hybrid Topology Optimization Method Of Simp And Mmc Considering Precise Control Of Minimum Size. *Chin. J. Theor. Appl. Mech.* **2022**, *54*, 3524–3537.
- Zhang, J.; Liao, J.; Liu, E. Topology optimization method based on SIMP-MMC for structure size precise control. *J. Mech. Strength* **2022**, *44*, 102–110.
- Cheng, G.; Jiang, Z. Study on topology optimization with stress constraints. *Eng. Optim.* **1992**, *20*, 129–148. [[CrossRef](#)]
- Cheng, G.D.; Guo, X. ϵ -relaxed approach in structural topology optimization. *Struct. Optim.* **1997**, *13*, 258–266. [[CrossRef](#)]
- Rozvany, G.; Sobieszczanski-Sobieski, J. New optimality criteria methods: Forcing uniqueness of the adjoint strains by corner-rounding at constraint intersections. *Struct. Optim.* **1992**, *4*, 244–246. [[CrossRef](#)]
- Kreisselmeier, G.; Steinhauser, R. Systematic control design by optimizing a vector performance index. In *Computer Aided Design of Control Systems*; Elsevier: Amsterdam, The Netherlands, 1980; pp. 113–117.
- Duysinx, P.; Sigmund, O. New developments in handling stress constraints in optimal material distribution. In Proceedings of the 7th AIAA/USAF/NASA/ISSMO Symposium on Multidisciplinary Analysis and Optimization, St. Louis, MO, USA, 2–4 September 1998; p. 4906.
- Yang, D.; Liu, H.; Zhang, W.; Li, S. Stress-constrained topology optimization based on maximum stress measures. *Comput. Struct.* **2018**, *198*, 23–39. [[CrossRef](#)]

16. Senhora, F.V.; Giraldo-Londono, O.; Menezes, I.F.; Paulino, G.H. Topology optimization with local stress constraints: A stress aggregation-free approach. *Struct. Multidiscip. Optim.* **2020**, *62*, 1639–1668. [CrossRef]
17. Zhai, X.; Chen, F.; Wu, J. Alternating optimization of design and stress for stress-constrained topology optimization. *Struct. Multidiscip. Optim.* **2021**, *64*, 2323–2342. [CrossRef]
18. da Silva, G.A.; Aage, N.; Beck, A.T.; Sigmund, O. Local versus global stress constraint strategies in topology optimization: A comparative study. *Int. J. Numer. Methods Eng.* **2021**, *122*, 6003–6036. [CrossRef]
19. Zhang, S.; Gain, A.L.; Norato, J.A. Stress-based topology optimization with discrete geometric components. *Comput. Methods Appl. Mech. Eng.* **2017**, *325*, 1–21. [CrossRef]
20. Zhang, W.; Li, D.; Zhou, J.; Du, Z.; Li, B.; Guo, X. A moving morphable void (MMV)-based explicit approach for topology optimization considering stress constraints. *Comput. Methods Appl. Mech. Eng.* **2018**, *334*, 381–413. [CrossRef]
21. Rostami, P.; Marzbanrad, J. Stress-limited topology optimization with local volume constraint using moving morphable components. *Arch. Appl. Mech.* **2021**, *91*, 2345–2367. [CrossRef]
22. Deng, J.; Chen, W. Design for structural flexibility using connected morphable components based topology optimization. *Sci. China Technol. Sci.* **2016**, *59*, 839–851. [CrossRef]
23. Guo, X.; Zhang, W.; Zhang, J.; Yuan, J. Explicit structural topology optimization based on moving morphable components (MMC) with curved skeletons. *Comput. Methods Appl. Mech. Eng.* **2016**, *310*, 711–748. [CrossRef]
24. Zheng, R.; Kim, C. An enhanced topology optimization approach based on the combined MMC and NURBS-curve boundaries. *Int. J. Precis. Eng. Manuf.* **2020**, *21*, 1529–1538. [CrossRef]
25. Wang, L.; Shi, D.; Zhang, B.; Li, G.; Liu, P. Real-time topology optimization based on deep learning for moving morphable components. *Autom. Constr.* **2022**, *142*, 104492. [CrossRef]
26. Li, Z.; Hu, X.; Chen, W. Moving morphable curved components framework of topology optimization based on the concept of time series. *Struct. Multidiscip. Optim.* **2023**, *66*, 19. [CrossRef]
27. Zhang, W.; Yuan, J.; Zhang, J.; Guo, X. A new topology optimization approach based on Moving Morphable Components (MMC) and the ersatz material model. *Struct. Multidiscip. Optim.* **2016**, *53*, 1243–1260. [CrossRef]
28. Ni, B.; Elishakoff, I.; Jiang, C.; Fu, C.; Han, X. Generalization of the super ellipsoid concept and its application in mechanics. *Appl. Math. Model.* **2016**, *40*, 9427–9444. [CrossRef]
29. Zhang, W.; Li, D.; Yuan, J.; Song, J.; Guo, X. A new three-dimensional topology optimization method based on moving morphable components (MMCs). *Comput. Mech.* **2017**, *59*, 647–665. [CrossRef]
30. Guo, H.; Zhao, K.; Wang, M.Y. A new approach for simultaneous shape and topology optimization based on dynamic implicit surface function. *Control Cybern.* **2005**, *34*, 255–282.
31. Shannon, T.; Robinson, T.; Murphy, A.; Armstrong, C. Generalized Bezier components and successive component refinement using moving morphable components. *Struct. Multidiscip. Optim.* **2022**, *65*, 193. [CrossRef]
32. Verbart, A.; Langelaar, M.; Keulen, F.v. A unified aggregation and relaxation approach for stress-constrained topology optimization. *Struct. Multidiscip. Optim.* **2017**, *55*, 663–679. [CrossRef]
33. Cui, T.; Sun, Z.; Liu, C.; Li, L.; Cui, R.; Guo, X. Topology optimization of plate structures using plate element-based moving morphable component (MMC) approach. *Acta Mech. Sin.* **2020**, *36*, 412–421. [CrossRef]
34. Du, Z.; Cui, T.; Liu, C.; Zhang, W.; Guo, Y.; Guo, X. An efficient and easy-to-extend Matlab code of the Moving Morphable Component (MMC) method for three-dimensional topology optimization. *Struct. Multidiscip. Optim.* **2022**, *65*, 158. [CrossRef]
35. Svanberg, K. The method of moving asymptotes—A new method for structural optimization. *Int. J. Numer. Methods Eng.* **1987**, *24*, 359–373. [CrossRef]
36. Zhang, W.S.; Guo, X.; Wang, M.Y.; Wei, P. Optimal topology design of continuum structures with stress concentration alleviation via level set method. *Int. J. Numer. Methods Eng.* **2013**, *93*, 942–959. [CrossRef]
37. Manual, A.S.U. Abaqus 6.11. 2012, Volume 89, v6. Available online: <http://130.149.89.49:2080/v2016/index.html> (accessed on 17 July 2024).
38. Jiang, X.; Wang, H.; Li, Y.; Mo, K. Machine learning based parameter tuning strategy for MMC based topology optimization. *Adv. Eng. Softw.* **2020**, *149*, 102841. [CrossRef]

Disclaimer/Publisher’s Note: The statements, opinions and data contained in all publications are solely those of the individual author(s) and contributor(s) and not of MDPI and/or the editor(s). MDPI and/or the editor(s) disclaim responsibility for any injury to people or property resulting from any ideas, methods, instructions or products referred to in the content.